

# Deformation and relaxation of viscous thin films under bouncing drops

Srinath Lakshman<sup>1</sup>†, Walter Tewes<sup>1</sup>, Jacco H. Snoeijer<sup>1</sup>, and Detlef Lohse<sup>1</sup>

<sup>1</sup>Physics of Fluids, Faculty of Science and Technology, University of Twente,  
7500AE Enschede, The Netherlands

(Received xx; revised xx; accepted xx)

Surfaces coated with thin and viscous liquids benefit from hydrodynamic lubrication desired in many applications. However, such surfaces are often subject to stressful conditions (eg. impacts, shearing), which can cause mild to violent deformations of the liquid film, thereby adversely affecting its performance capabilities. Here we investigate free surface oil film deformations that arise due to the air pressure buildup under impacting and rebounding water drops. Using Digital Holographic Microscopy, we measure the 3D surface topography of the deformed film immediately after the drop rebound, with a resolution down to 20 nanometers. We first discuss how the film is initially deformed during impact, as a function of film thickness, film viscosity, and drop impact speed. Subsequently, we describe the slow relaxation process of the deformed film after the rebound. Scaling laws for the broadening of the width and the decay of the amplitude of the perturbations are obtained experimentally, which are in excellent agreement with a lubrication analysis. Thereby the work offers a detailed spatio-temporal description of the oil film deformations that arise during the impact and rebounding of water drops.

## 1. Introduction

Drops impacting a liquid layer occur in nature as well in many industrial and technological applications. Common examples are raindrops hitting the surface of a pond, spray coating on a wet substrate or inkjet printing on a primer layer. The collision can generate complex scenarios such as floating, bouncing, splashing, jetting, which have been extensively studied (Worthington 1908; Rein 1993; Weiss & Yarin 1999; Thoroddsen *et al.* 2008). Impact velocity, impact angle, droplet size, liquid layer thickness, etc. are some of the key parameters which influence the impact. Among the many different impact scenarios, a particularly intriguing phenomenon is reported to occur at sufficiently low impact velocities: floating or bouncing drops which never directly contact the underlying liquid. The earliest observation of a drop floating over a liquid surface was made by Reynolds (1881) who noticed that under certain circumstances, the drops spraying from the bow of a boat or droplets from a shower of raindrops float on liquid surfaces for some seconds before they disappear. Later, Rayleigh (1882) reported bouncing of drops when collision of two distinct streams of liquids resulted in, under certain circumstances, drops bouncing off each other without merging. The reason for the presence of repulsion forces on impacting droplets even without direct contact with the (liquid) substrate is a lubrication pressure build-up in the draining thin air layer between droplet and substrate which was first detailed in the theoretical work by Smith *et al.* (2003). The importance of such thin air layers sparks interest in numerous recent

† Email address for correspondence: srinathl@utwente.nl

investigations of eg., skating drops (Mandre *et al.* 2009; Hicks & Purvis 2010, 2011; Kolinski *et al.* 2012, 2014), entrapment of bubbles (Thoroddsen *et al.* 2003, 2005; Tran *et al.* 2013; Hendrix *et al.* 2016), dimple formation under a falling drop (van der Veen *et al.* 2012; Duchemin & Josserand 2012; Li & Thoroddsen 2015), and suppressing of splash (Xu *et al.* 2005). Floating/bouncing drops can be observed not only on liquid surfaces but also on dry surfaces. Such scenarios include drops bouncing on a dry surface (Kolinski *et al.* 2012; De Ruiter *et al.* 2012; Kolinski *et al.* 2014), drops floating on a very hot surface (Leidenfrost effect) (Chandra & Avedisian 1991; Quéré 2013), drops bouncing on a pool of liquid (Rodriguez & Mesler 1985; Klyuzhin *et al.* 2010), drops floating/bouncing on a vibrating pool of liquid (Couder *et al.* 2005*a,b*), and drops floating on a very cold pool of liquid (inverse Leidenfrost effect) (Gauthier *et al.* 2019*a,b*).

An important parameter for the study of drops bouncing on liquid layers is the height  $h_f$  of the latter above an underlying solid substrate as compared to the drop radius  $R_w$ . Experiments by Pan & Law (2007) reveal drop bouncing to be favoured on deep pools  $h_f > R_w$  as compared on thick  $h_f \approx R_w$  and on thin films  $h_f < R_w$ . It was argued that the solid substrate (wall) restricts the penetration of the falling drop in thin-films thereby suppressing bouncing. For thin films, the bouncing phenomenon is only observed for drops having moderately low kinetic energy as compared to their surface energy, i.e.,  $We = \rho_w R_w v_w^2 \gamma_w^{-1} \lesssim 10$ , where  $\rho_w$  is the density of the drop,  $v_w$  is the drop impact speed and  $\gamma_w$  is the surface tension of the drop. At sufficiently high impact velocities, the drop contacts the underlying liquid due to Van der Waals attraction force between the two liquids which becomes important when the liquid-liquid separation is smaller than around 100 nm (Charles & Mason 1960). The critical Weber number which marks the transition from drop bouncing to merging has been studied by Tang *et al.* (2018) using liquids of different viscosities. They found that the critical Weber number increases as viscosity of the droplet and thin film are increased which indicates that larger viscosity liquids promotes drop bouncing. A similar observation is seen in the work of Langley & Thoroddsen (2019), where delayed coalescence is observed for drops and thin films with large viscosities. Gilet & Bush (2012) and Hao *et al.* (2015) found drop bouncing on a thin film to be similar to bouncing on a super-hydrophobic substrate. One such similarity was the apparent contact time of the drop which agreed well with the Hertz contact time (Richard *et al.* 2002). However, the droplet-film collision resembled an almost elastic collision between the two liquids with the coefficient of restitution close to unity. Pack *et al.* (2017); Lo *et al.* (2017); Tang *et al.* (2019) used interferometry measurements to obtain the time-resolved evolution of nanometric profiles of the air gap between impacting drops and thin viscous layers. They found a bell shaped annular air profile with maximum thickness at the center and the minimum thickness at a radially outwards location which varied with time. Small variations in air profiles were observed when the impacting drop was slightly oblique relative to the underlying film surface and when the film thickness was increased from thin film to a deep pool limit. Significant asymmetries were also observed in the evolution of air profiles when comparing the drop spreading stage to the receding stage for a typical bounce process. Lo *et al.* (2017) successfully measured both the drop and the thin film deformations during the approach process. However, the deformations could only be obtained at a single time instance by performing two separate experiments under identical impact conditions.

Previous experimental and numerical studies of drop bouncing on thin films mainly focused either on the macroscopic drop bouncing behaviour or on the evolution of the nanometric gas thickness between the two liquids without providing a distinction

between drop and thin film deformations. The experimental studies ignore the thin film deformations owing to the small film thickness and large film viscosity used in the experiments (Pack *et al.* 2017; Gilet & Bush 2012) which is assumed to mimic a smooth solid surface. The numerical studies of thin film deformations prove challenging because of the large difference in involved length scales (millimetric to nanometric deformations) when computing the lubrication gas flow and the thin film flow simultaneously to drop deformations (Josserand & Zaleski 2003). Although viscous thin film deformations are typically small, they cannot be discounted since they play a crucial role in modulating the gas thickness thereby affecting drop bouncing process and possibly the coalescence of drop and thin film at higher impact velocities. The thin film deformations can also give clues on the size and the velocity of the impacted drop much alike how impact craters are used to determine the size and velocity of the impacted body. Finally, understanding the size and structure of the thin film deformations is very useful in the development of slippery surfaces eg. Liquid Infused Surfaces (LIS), Lubricant Infused Slippery Surfaces (LubISS), which suffers from liquid/lubricant depletion through shearing, cloaking, and depletion in the wetting ridges (Schellenberger *et al.* 2015; Teisala *et al.* 2018; Baumli *et al.* 2019).

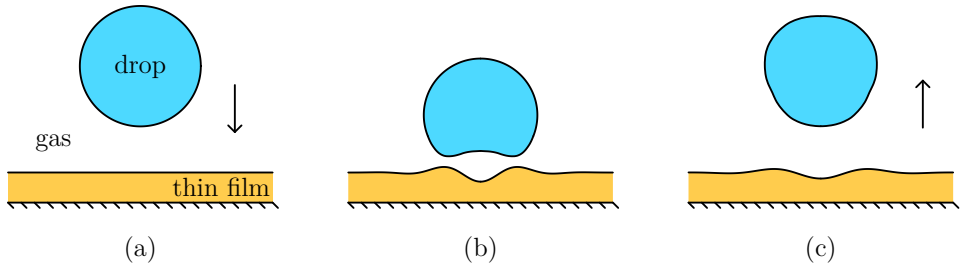


Figure 1: Schematic diagram (not to scale) of a drop bouncing on a thin film in a surrounding gas environment. Three stages in the bounce process are shown: (a) Prior to impact, (b) during the bounce, where both the droplet and the oil film deform, (c) after the bounce, where the oil deformations slowly relax.

A schematic diagram of a drop bouncing on a thin liquid film is shown in figure 1. We highlight three important stages of a drop bouncing scenario. (a) Initial stage (cf. Figure 1a) - A drop falls towards a flat film surface in a surrounding gas medium. (b) Deformation stage (cf. Figure 1b) - The drop's center of mass velocity changes direction due to the lubrication force provided by the narrow gas layer separating the two liquids which exceeds the droplet's weight. Large spatial variations of the gas pressure cause large drop and significant thin film deformations in this stage. (c) Relaxation stage (cf. Figure 1c) - The drop is far from the film surface after the bounce. The gas pressure separating the two liquids is again reduced to ambient pressure and the thin film deformations gradually decay via an intricate relaxation process.

In this paper, we investigate the thin oil film deformations caused by impacting water drops at  $We \sim 1$ . First, in section 2, the experimental setup and the control parameters are described and some typical orders of magnitude of the relevant non-dimensional numbers are given. The subsequently presented results are twofold: In section 3, we discuss the film surface deformations immediately after the bouncing event. We quantify

how the surface deformations depend on the film thickness, film viscosity and drop impact speed. This part of the paper describes the deformations of the thin film after the end of the deformation stage (cf. Figure 1b). The second part of our study is presented in section 4 and focusses on the relaxation stage described above (cf. figure 1c). We first illustrate a typical relaxation process of film deformations which occurs after the drop bouncing. Starting from experimentally obtained deformations as initial conditions, we then compare the evolution of the experimental profiles in the relaxation process to a numerical calculation using lubrication theory. Next, we use a general theoretical result of [Benzaquen et al. \(2015\)](#) for the relaxation of thin film deformations. The thus obtained scaling laws for the width broadening  $\lambda(t)$  and amplitude decay  $\delta(t)$  during the relaxation process are compared to our experiments over a large range of parameters. Finally, the paper closes with a Discussion in section 5.

## 2. Experimental details

A schematic drawing of the experimental setup is shown in figure 2. Using a syringe pump, Milli-Q water is slowly dispensed out of a needle tip as soon as the droplet's weight overcomes the surface tension force. The detached water droplet of radius  $R_w = 1.08\text{ mm}$  is made to fall on a thin and viscous silicone oil film. The 3D surface topography of the deformed oil film is measured using a digital holography technique, as described below, complemented by simultaneous side view visualisations of the drop dynamics. The silicone oil films are prepared by the method of spin coating on cleaned glass slides. The film thickness is measured by the use of a white light spectrometer. Table 1 gives the density, dynamic viscosity, and surface tension of different liquids used in the present study. The density and dynamic viscosity of air at standard temperature and pressure are  $\rho_a \approx 1.2\text{ kg/m}^3$  and  $\eta_a \approx 0.002\text{ mPa.s}$ , respectively. The film deformations are measured by varying three important control parameters, namely the oil film thickness  $h_f$  which is either about  $5\text{ }\mu\text{m}$ ,  $10\text{ }\mu\text{m}$ , or  $15\text{ }\mu\text{m}$ , the oil film viscosity  $\eta_f$  which is either  $52\text{ mPa.s}$ ,  $98\text{ mPa.s}$ , or  $186\text{ mPa.s}$ , and the impacting water droplet speed  $v_w$ , for which we choose  $0.16\text{ m/s}$  or  $0.37\text{ m/s}$ .

Liquids	Density $\rho$ [ $\text{kg/m}^3$ ]	Dynamic viscosity $\eta$ [ $\text{mPa.s}$ ]	Surface tension $\gamma$ [ $\text{mN/m}$ ]
Water $(w)$	995	1	72
Silicone oils $(f)$	959	52	20
	950	98	19
	963	186	19

Table 1: Properties of liquids used in the experiments. Subscripts  $w$  and  $f$  represent water and oil-film respectively. Symbol  $\gamma$  represents liquid-air surface tension.

For the measurement of film deformations, a holographic technique is used ([Gabor 1949; Schnars et al. 2016](#)). The Digital Holographic Microscopy (DHM®-R1000 by Lyncée Tec) device provides real-time measurements of (at least)  $20\text{ nm}$  vertical resolution within the  $200\text{ }\mu\text{m}$  measuring window (for details refer Appendix A). A 2.5x objective is used along with the DHM setup, which provides a roughly  $4.90\text{ }\mu\text{m}$  lateral resolution and allows for measurements of a maximum deformation slope up to  $2^\circ$ . A

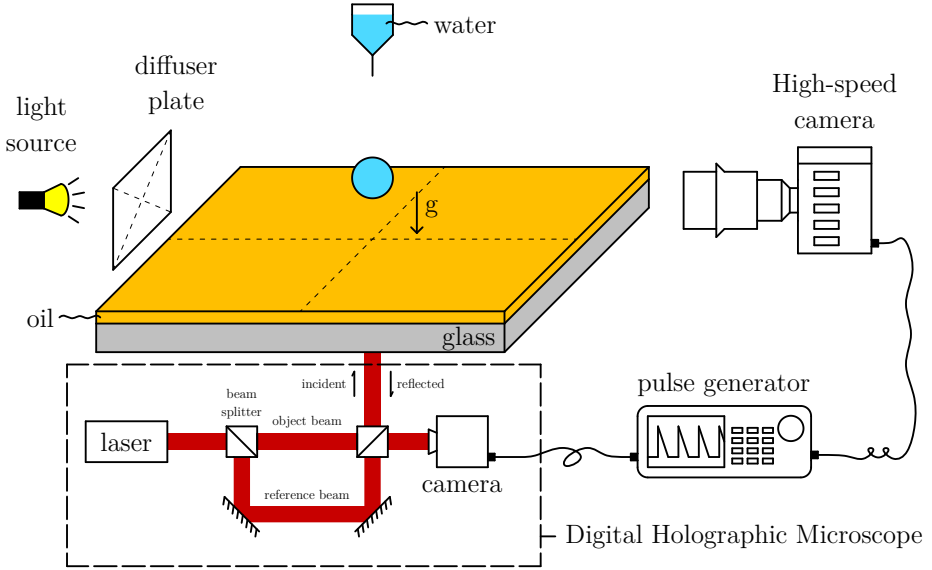


Figure 2: Schematic diagram (not to scale) of the experimental setup. Bottom view: Holographic setup, positioned underneath the glass substrate. It is used to measure free surface oil film deformations. Side view: The dynamics of impacting water drop is characterised using a high speed camera.

pulse generator connects and synchronizes the recordings of the side view camera and the DHM camera at a temporal resolution of around 0.5 kHz.

Deformation	Relaxation
$We = \rho_w R_w v_w^2 \gamma_w^{-1} \sim 1$	$Re_f = \rho_f h_f \gamma_f \eta_f^{-2} \sim 10^{-2}$
$Re_w = \rho_w R_w v_w \eta_w^{-1} \sim 10^{+2}$	$\eta^* = \eta_f \eta_w^{-1} \sim 10^{+2}$
$Re_a = \rho_a R_w^{1/2} h_a^{1/2} v_w \eta_a^{-1} \sim 10^{-1}$	$h^* = h_f R_w^{-1} \sim 10^{-2}$

Table 2: Relevant dimensionless numbers and their orders of magnitude for both the deformation and the relaxation stage. Subscripts  $w$ ,  $a$  and  $f$  represent water, air and oil-film respectively.

Given the experimental parameters stated in this section, the orders of magnitude of the relevant dimensionless numbers are summarized in table 2. The dimensionless numbers are useful to identify some qualitative flow features for the deformation stage (cf. figure 1b) and the relaxation stage (cf. figure 1c) pertaining to drop bouncing. For the deformation stage, the low value of  $We \sim 1$  causes drops to bounce on viscous thin films (Hao *et al.* 2015; Lo *et al.* 2017; Pack *et al.* 2017; Tang *et al.* 2019).  $Re_w \sim 10^{+2}$  indicates a potential flow inside the falling drop independent of the substrate underneath

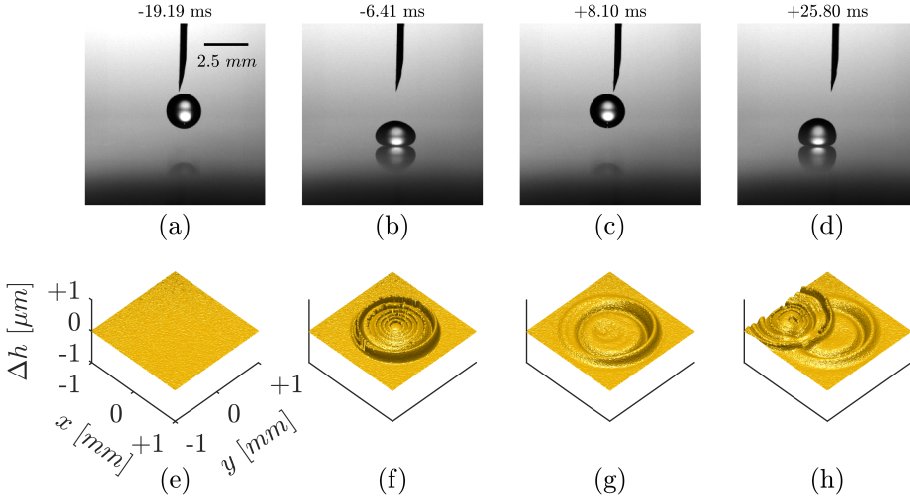


Figure 3: Snapshots of a water drop bouncing on an oil film. Drop bouncing behaviour shown in the first row (a) – (d). Evolution of the oil-air deformation shown in the second row (e) – (h). Location of impact center is  $[x, y] = [0, 0]$  mm. Control parameters used,  $We = 0.38$ ,  $h^* = 0.01$  and  $\eta^* = 98$ .

(Moláček & Bush 2012; Hendrix *et al.* 2016).  $Re_a = \rho_a L_a v_a \eta_a^{-1} \sim 10^{-1}$  indicates a viscous squeeze flow in thin air gaps during impact, using  $L_a \sim R_w^{1/2} h_a^{1/2}$ ,  $v_a \sim v_w$  as the velocity scale (Mandre *et al.* 2009) and  $h_a \sim 1 \mu\text{m}$  (van der Veen *et al.* 2012). For the relaxation stage,  $Re_f = \rho_f L_f v_f \eta_f^{-1} \sim 10^{-2}$  indicates a Stokes flow, using  $L_f \sim h_f$  and  $v_f \sim \gamma_f \eta_f^{-1}$  (Salez *et al.* 2012). Here,  $\eta^* \sim 10^{+2}$  and  $h^* \sim 10^{-2}$  suggests small amplitude thin film perturbations due to small film thickness in comparison with the lateral length scales ( $h_f \ll R_w$ ). Drop size and film thickness are much below the capillary length, so that gravity can be neglected.

### 3. Deformation of viscous thin films

#### 3.1. Typical bouncing experiment

Before turning to a detailed quantitative analysis, we first describe the oil film deformations observed in a typical experiment. The synchronized recordings of the drop bouncing using a high speed camera and the oil surface deformation measured using DHM are shown in the respective top and bottom rows in figure 3.

When the falling water drop is still far from the oil-air interface, the droplet takes on a spherical shape while there is no deformation in the oil surface (figure 3(a) & 3(e)). As the bottom of the falling water drop approaches the oil-air interface, the air pressure builds up in the narrow air gap, deforming both the water-air and oil-air interface. The lubrication air pressures in narrow air gaps can become sufficiently large to decelerate the falling drop, bringing it to rest (or in apparent contact with the oil-air interface) and cause a reversal in droplets momentum, leading to a contact-less drop bouncing. The maximum drop spreading and the corresponding oil-air deformation obtained during the apparent contact is shown in figure 3(b) & 3(f). It should be noted that during this phase the holography measurement cannot be trusted quantitatively. This is due

to the fact that when the drop is too close to the oil-air interface (small air gaps,  $h_a \lesssim 100 \mu\text{m}$ ), additional light reflections from the water-air interface interfere with the measurements of the oil-air interface (for details refer to Appendix A). However, As soon as the drop has bounced back and is sufficiently far away from the oil-air interface (large air gaps,  $h_a \gtrsim 100 \mu\text{m}$ ), light reflections from the water-air interface are no longer present, and the measurements of the oil-air interface are quantitatively accurate. A snapshot of the drop bounced off far away from the oil-air interface and the corresponding oil-air deformation are shown in figure 3(c) & 3(g). Subsequent to this, the oil film relaxes towards a flat state under the influence of surface tension, until it is again perturbed by a second impact of the rebounding drop (Figure 3(d) & 3(h)).

Figure 4(a) presents a typical surface topography of the oil-air interface after the bounce. The corresponding azimuthally averaged deformation profile is shown in figure 4(b), where in this case the average is performed over the full annulus within  $0 \leq \theta < 2\pi$ . In the remainder, we choose  $t = 0$  as the earliest time when clean DHM measurements are obtained after the drop bounce off process (cf. Appendix A). Figure 4(a) shows that deformations are highly localised, within a narrow annulus  $r_{an} \approx 0.6 - 0.8 \text{ mm}$ . Given that flow inside the viscous film requires pressure gradients, such localised deformations suggest that spatial variations of air pressure during the bounce are highly localised during impact (figure 1(b)). The appearance of such an annulus is reminiscent of dimple formation underneath an impacting drop: An annular local minimum of the air gap is seen for drops impacting a dry substrate (Mandre *et al.* 2009; Hicks & Purvis 2010; Kolinski *et al.* 2012; van der Veen *et al.* 2012; Bouwhuis *et al.* 2012), drops impacting a thin liquid film (Hicks & Purvis 2011) and drops impacting a liquid pool (Hendrix *et al.* 2016). We therefore hypothesize that the radial location of the deformation correlates to the minimum of the air gap during drop impact.

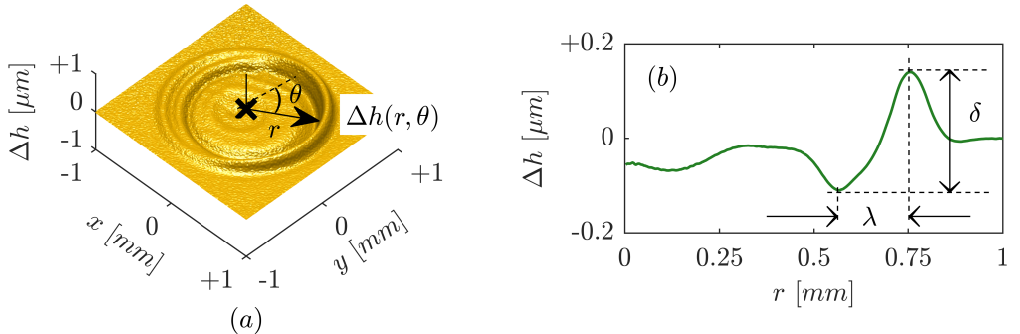


Figure 4: (a) Surface topography of the oil-air interface at  $t = 0$ . (b) Azimuthally averaged deformation profile over the full annulus at  $t = 0$ . We define the wave characteristics  $\delta$  (amplitude) and  $\lambda$  (wavelength). Control parameters used:  $We = 0.38$ ,  $h^* = 0.01$  and  $\eta^* = 98$ .

In the present experiments, the oil surface deformations at  $t = 0$  are not perfectly axisymmetric (see figure 4(a)). This small asymmetry is attributed to a small horizontal impact speeds, which is difficult to eliminate experimentally. This small horizontal speed affects the air layer thickness during the bounce process (Lo *et al.* 2017), leaving asymmetric imprint on the oil layer. In the remainder we will average the profiles only

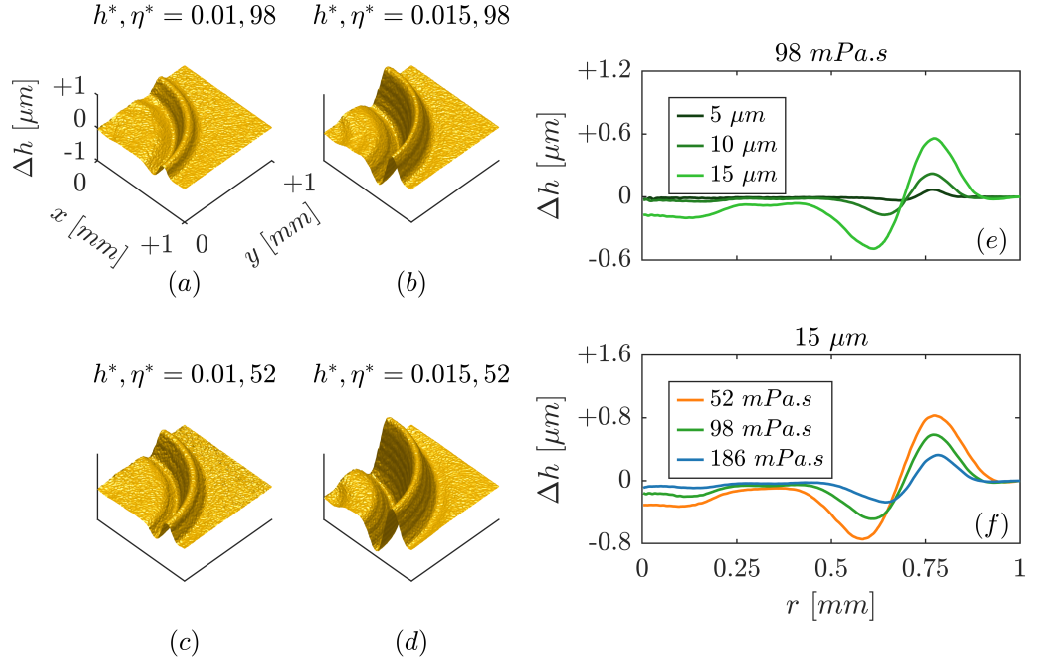


Figure 5: (a) - (d) Surface topographies of the oil-air interface at  $t = 0$  in a quadrant  $0 \leq \theta < \pi/2$ . (e) & (f) Azimuthally averaged deformation profile over the quadrant at  $t = 0$ . Control parameters used:  $We = 0.38$ ,  $h^* = h_f/R_w = \{0.005, 0.01, 0.015\}$  and  $\eta^* = \eta_f/\eta_w = \{52, 98, 186\}$ .

over one quadrant. Finally, we remark that figure 4b defines two quantities that will be used below to characterise the wave: the amplitude  $\delta$  and the wavelength  $\lambda$ , respectively defined as the vertical and horizontal distance from the minimum to the maximum of the film.

### 3.2. Influence of film properties and drop impact velocity

We now study the influence of the film thickness and the film viscosity on the surface deformations left behind after impact. Figures 5(a) - 5(d) show the surface topographies at  $t = 0$  in one quadrant. Figures 5(e) and 5(f) show the corresponding azimuthally averaged deformation profiles at  $t = 0$ , averaged over the quadrant. Clearly, a decrease in deformation amplitude  $\delta$  is seen with a decrease in initial film thickness (cf. rows in figure 5(a) - 5(d) and figure 5(e)). On the other hand, a decrease in deformation amplitude is seen with an increase in film viscosity (cf. columns in figure 5(a) - 5(d) and figure 5(f)). To further quantify this, we plot the initial amplitude  $\delta_0 = \delta(t = 0)$  as functions of film thickness and film viscosity in Figure 6(a) and 6(b). From these plots we empirically deduce that the initial amplitude scales as  $\delta_0 \sim h_f^2 \eta_f^{-1}$ . This scaling is not immediately obvious, since the “mobility” of a thin layer flow is known to scale as  $h_f^3/\eta_f$ . *Jacco: I do not see how to improve on this; I would have expected  $h_f^3/\eta_f$ ... but the data are better aligned with  $h_f^2/\eta_f$ . Perhaps we should speculate on the coupling with the air flow.*

Next, we study the influence of the impact velocity on the surface deformations left behind after impact. Figures 7(a) & 7(b) show the surface topographies at  $t = 0$  for two

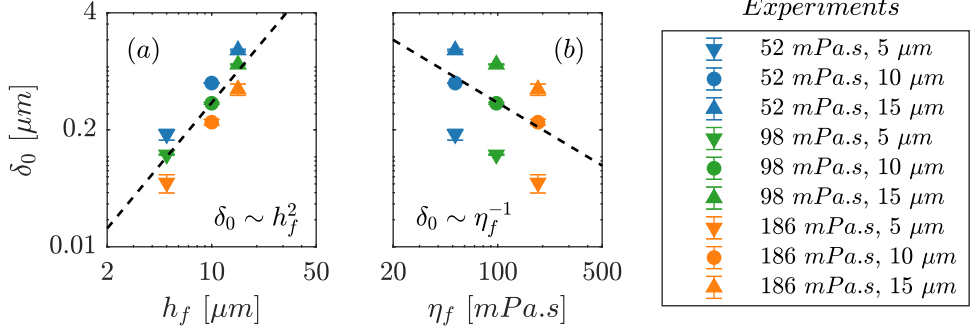


Figure 6: Scaling of the initial amplitude with film thickness and film viscosity. Control parameters used:  $We = 0.38$ ,  $h^* = h_f/R_w = \{0.005, 0.01, 0.015\}$  and  $\eta^* = \eta_f/\eta_w = \{52, 98, 186\}$ .

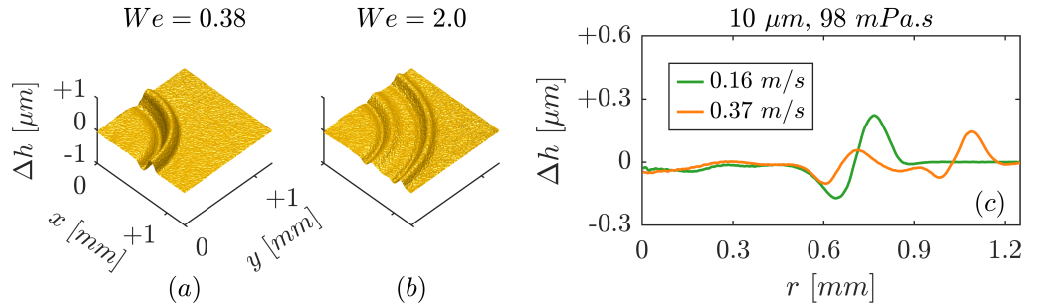


Figure 7: (a) - (b) Surface topographies of the oil-air interface at  $t = 0$  in a quadrant  $0 \leq \theta < \pi/2$ . (c) Azimuthally averaged deformation profile over the quadrant at  $t = 0$ . Parameters used:  $We = \{0.38, 2.0\}$ ,  $h^* = h_f/R_w = 0.01$  and  $\eta^* = \eta_f/\eta_w = 98$ .

different impact velocities. Figure 7(c) shows the corresponding azimuthally averaged deformation profiles. For the higher impact velocity (Figure 7(b)), two distinct peaks in deformation are observed – we emphasise that the profile corresponds to a single impact. This is in contrast with the single peak that appears at lower velocity (Figure 7(a)). Moreover, the deformations are more radially spread out for the higher impact speed as compared to lower impact speed. The transition from one peak to two peaks and the increased radial spread is reminiscent of the transition from single dimple to double dimple formation in a falling drop, as previously observed on dry surfaces (De Ruiter *et al.* 2012; de Ruiter *et al.* 2015). This again suggests that the deformation directly reflects the structure of the dimple below the impacting drop.

## 4. Relaxation of viscous thin film deformations

### 4.1. Spacetime plot of typical relaxation process

We now reveal the relaxation of viscous thin film deformations after the impact process. When the drop is far away from the film surface after the bounce, the air pressure is again homogeneous and no longer provides any forcing to the film. By consequence film deformations gradually decay via an intricate relaxation process, under the influence of surface tension. Figure 8 provides a spacetime plot of a typical

relaxation process, over two decades in time ( $t \sim 0.01 - 1 \text{ s}$ ). The figure corresponds to an azimuthal average of surface deformation within a quarter annulus ( $0 \leq \theta < \pi/2$ ). The lines indicate the loci of deformation maxima (orange), minima (blue) and zero-crossing (green). These lines highlight that the deformation involves a decay in amplitude as well as a broadening of the lateral width of the deformation profile. Note that during this process, the position of the zero crossing (green line) remains approximately constant.

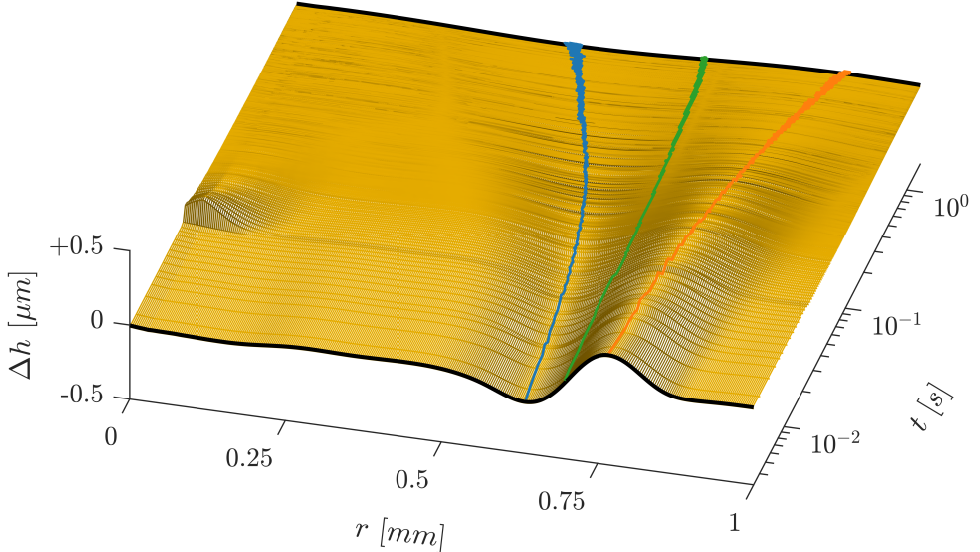


Figure 8: Spacetime plot of the relaxation process. Initial and final deformations are plotted as black lines. Loci of deformation maxima, minima and zero crossings are plotted as orange, blue, and green lines, respectively. A secondary deformation occurs at  $t \approx 0.1 \text{ s}$  near the impact center due to the next impact process. Control parameters used:  $We = 0.38$ ,  $h^* = h_f/R_w = 0.01$  and  $\eta^* = \eta_f/\eta_w = 98$ .

#### 4.2. Numerical simulation

We perform numerical simulations in order to study the relaxation process of the viscous thin films. The relaxation process is modelled using lubrication theory (Reynolds 1886; Oron *et al.* 1997). Lubrication theory relies on the following conditions, which are indeed satisfied in the experiment, namely, (i) viscous forces in the film dominate over inertial forces ( $Re_f \sim 10^{-2} \ll 1$ ) and (ii) deformation amplitudes in vertical direction are much lower than the characteristic lateral length scale ( $\delta/\lambda \sim 10^{-2} \ll 1$ ). As boundary conditions we consider the free surface to be in contact with a homogenous gas pressure, as is the case after rebound, while there is a no-slip boundary condition at the substrate. The corresponding lubrication (thin film) equation reads (Oron *et al.* 1997):

$$\partial_t h + \frac{\gamma_f}{3\eta_f} \vec{\nabla} \cdot \left\{ h^3 \vec{\nabla} (\vec{\nabla}^2 h) \right\} = 0, \quad (4.1)$$

where,  $h(x, y, t)$  is the vertical distance between the solid substrate and the free surface and  $\vec{\nabla}$  is the two-dimensional gradient operator in the x-y plane. We perform a nondimensionalisation of (4.1) by  $h = h_f H$ ,  $r = h_f R$  and  $t = (3\eta_f h_f \gamma_f^{-1})T$ , where  $h_f$  is the initial film thickness. In the following, we will study the relaxation process in an

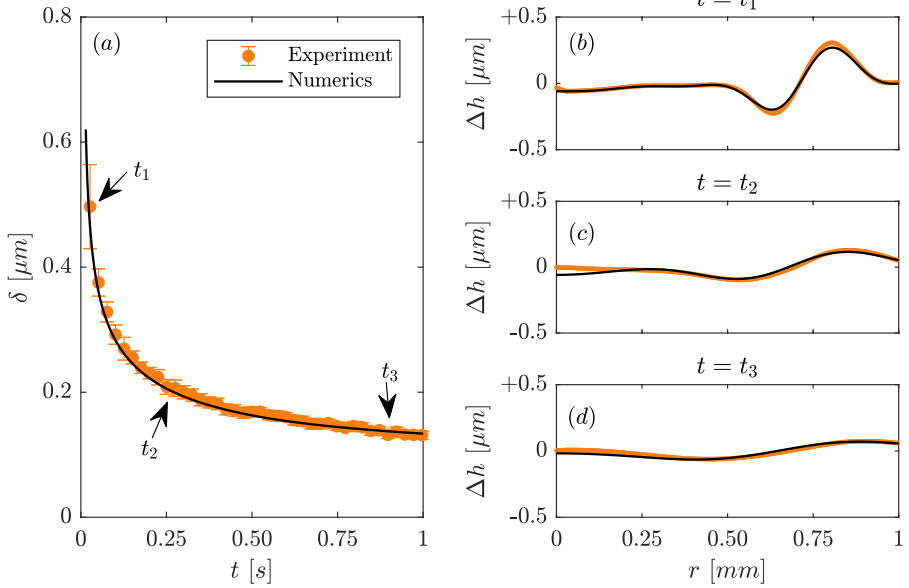


Figure 9: (a) Comparison of amplitude decay between experiment and numerics. (b – d) Comparison of film deformation between experiment and numerics at  $t_1 = 14\text{ ms}$ ,  $t_2 = 252\text{ ms}$  and  $t_3 = 966\text{ ms}$ . Control parameters used,  $We = 0.38$ ,  $h^* = 0.01$  and  $\eta^* = 52$ .

axisymmetric geometry, i.e.  $H = H(R, T)$  such that (4.1) becomes :

$$\partial_T H + \frac{1}{R} \partial_R \left[ R H^3 \left( \partial_R^3 H + \frac{1}{R} \partial_R^2 H - \frac{1}{R^2} \partial_R H \right) \right] = 0. \quad (4.2)$$

Importantly, (4.2) is devoid of any free parameters. To compare to experiment, we perform numerical simulations of film relaxation using a finite element method (implemented using the framework DUNE-PDELAB by Bastian *et al.* (2008b,a, 2010)). The deformation profile at  $t = 0$  is taken from the experiment and used as an initial condition, and subsequently the film profile is evolved via numerical integration of (4.2). A direct comparison between the experiments and the lubrication theory is given in figure 9 without any adjustable parameters. Figure 9(a) shows the amplitude  $\delta$  (defined as the difference between maximum and minimum of  $\Delta h$ ) as a function of time, while Figure 9(b) shows the deformation profiles  $\Delta h = h(r, t) - h_f$  at different times. The comparison exhibits very good agreement between the experiment and the numerical calculations, demonstrating the success of the lubrication approximation to describe the experimentally observed relaxation.

#### 4.3. Theoretical analysis

Now we turn to a detailed theoretical analysis of the relaxation process, from which we will establish the general scaling laws of the relaxation. To do this, we reduce the lubrication equation to a one-dimensional geometry  $h = h(x, t)$ . Here, we use  $X = x/h_f$  analogous to  $R = r/h_f$ . The rationale behind choosing a 1D lubrication equation is that the initial deformations are far from the impact center (see figure 5). This is further quantified in figure 8, where the “width” of the profile is initially an order of magnitude smaller than the location of the zero crossing. Therefore the axisymmetric relaxation and a one-dimensional relaxation will yield very similar results – at least until

the deformations approach the impact center and the azimuthal contributions become important.

The one-dimensional lubrication equation reads

$$\partial_T H + \partial_X (H^3 \partial_X^3 H) = 0. \quad (4.3)$$

To further simplify the analysis, we use the fact seen in the experiments that the deformation amplitudes are small in comparison to initial film thicknesses ( $\delta/h_f \sim 0.05 \ll 1$ ). This allows us to linearise (4.3) employing the variable transformation  $Z = h/h_f - 1 = H - 1$  where  $|Z| \ll 1$ . The linearised 1D lubrication equation then reads

$$\partial_T Z + \partial_X^4 Z = 0. \quad (4.4)$$

The relaxation of localised thin film perturbations described by (4.4) was analysed in great detail by Benzaquen *et al.* (2013, 2014, 2015); Bertin *et al.* (2020). They obtained the long time asymptotic solution in terms of a moment expansion,

$$Z(X, T) = \frac{\mathcal{M}_0 \phi_0(U)}{T^{1/4}} + \frac{\mathcal{M}_1 \phi_1(U)}{T^{2/4}} + \frac{1}{2} \frac{\mathcal{M}_2 \phi_2(U)}{T^{3/4}} - \dots, \quad (4.5)$$

which involves the similarity variable

$$U = XT^{-1/4}, \quad (4.6)$$

and similarity functions  $\phi_n(U)$  that can be determined analytically (Benzaquen *et al.* 2013, 2014, 2015). The amplitudes  $\mathcal{M}_n$  appearing in (4.5) can be determined from the initial condition  $Z_0(X) = Z(X, 0)$ , by computing the moments

$$\mathcal{M}_n = \int \xi^n Z_0(\xi) d\xi, \quad n = 0, 1, 2, \dots \quad (4.7)$$

It is clear from (4.5) and the similarity variable (4.6) that the width  $\lambda$  of the profile follows a universal scaling of the form  $\lambda \sim T^{1/4}$ . The decay of the amplitude  $\delta$  is more subtle, since each term in (4.5) decays differently, as  $\delta \sim T^{-(n+1)/4}$  for the  $n$ th moment. At late times, the solution  $Z(X, T)$  thus converges towards the lowest order term with a non-zero moment. Generically, for  $\mathcal{M}_0 \neq 0$ , the amplitude will therefore decay as  $1/T^{1/4}$ . In our case, however, the perturbation originates from an initially flat film, and by incompressibility of the layer, the perturbation is thus expected to have a vanishing volume, i.e.  $\mathcal{M}_0 = 0$ . In the present context, the lowest order moment is therefore expected to be  $\mathcal{M}_1 \neq 0$ . In this scenario, the scaling law will be  $\delta \sim 1/T^{1/2}$ , while the solution  $Z(X, T)$  should converge to  $\phi_1(U)$  for a zero volume perturbation. A schematic depiction of the approach to the  $\phi_1(U)$  attractor is shown in figure 10.

To verify this scenario, we turn to an exemplarily initial deformation profile of a 100 mPa.s, 10  $\mu\text{m}$  film, and probe the subsequent relaxation. For the specific example, the two lowest order moments are determined as  $\mathcal{M}_0 \approx 6.4 \times 10^{-2}$  and  $\mathcal{M}_1 \approx 3.2$ . The very small value of  $\mathcal{M}_0$  is of the order of the experimental resolution (i.e. it corresponds to a typical  $\Delta h \sim \pm 10 \text{ nm}$ ), so that indeed the perturbation has a negligible volume. Figure 11 reveals that the relaxation is indeed governed by  $\mathcal{M}_1$ , and approaches the  $\phi_1(U)$  self-similar attractor function. The figure reports the scaled deformation profiles centred around the zero crossing location  $X_0 \approx 69.7$ . The first row shows the deformation profile scaled with the initial film thickness. The second row shows the rescaled deformation profiles (vertical scale  $\sim 1/T^{1/2}$  and horizontal scale  $\sim T^{1/4}$ ). During late times, the rescaled deformation profiles clearly approach the attractor function  $\phi_1(U)$ , which is superimposed on the data. This excellent match confirms that, within the experimental

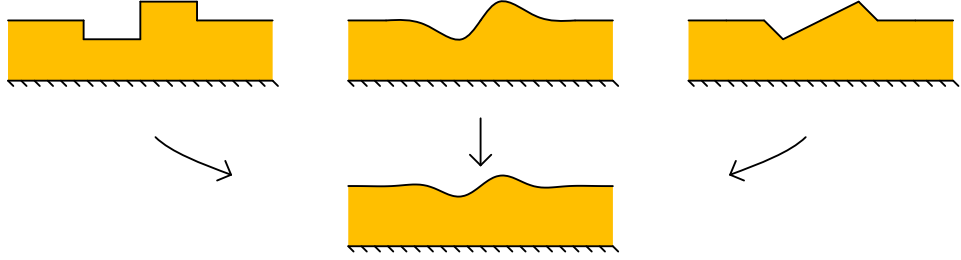


Figure 10: Schematic illustrating of the approach to the attractor function  $\phi_1(U)$ . The initial deformations are zero volume perturbations having moments  $\mathcal{M}_0 = 0$  and  $\mathcal{M}_1 \neq 0$ . Adapted from Benzaquen *et al.* (2014, 2015).

times, the axisymmetric effects have not yet started to contribute and the theoretical analysis of the film relaxation process over a 1D geometry is sufficient to understand the relaxation process in the experiments.

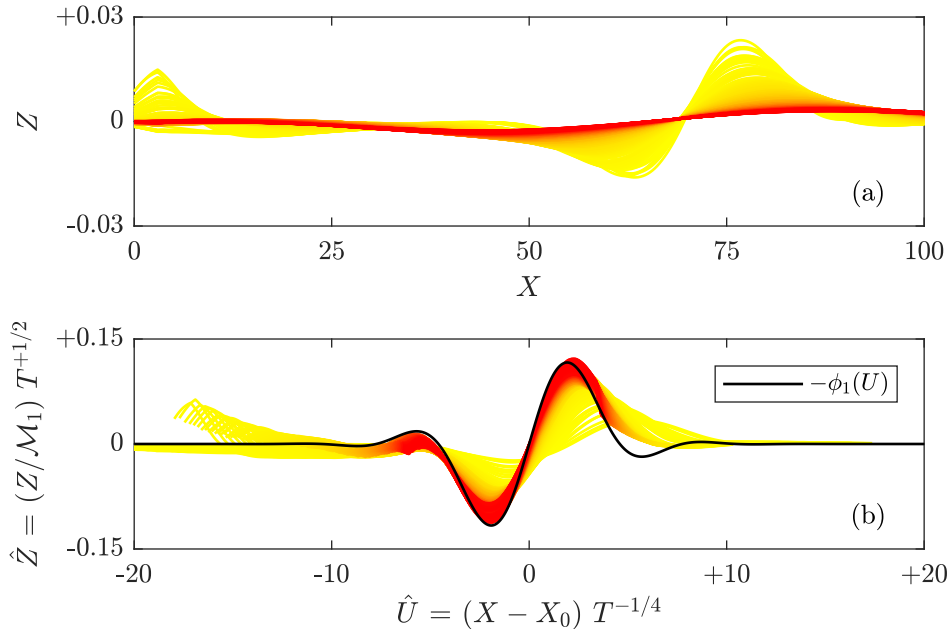


Figure 11: (a) Time evolution of the normalized deformation profiles  $Z$  vs  $X$ . (b) Time evolution of the scaled normalized deformation profiles  $\hat{Z}$  vs  $\hat{U}$ . The self-similar attractor function  $\phi_1(U)$  is plotted as a black line. Here,  $X_0 \approx 65$  and  $\mathcal{M}_1 \approx 3.2$ . The scaled and rescaled deformations are color coded with time; yellow to red as time increases. Control parameters used,  $We = 0.38$ ,  $h^* = 0.01$  and  $\eta^* = 98$ . **we need to change  $-\phi_1$  to  $\phi_1$  in the figure legend.**

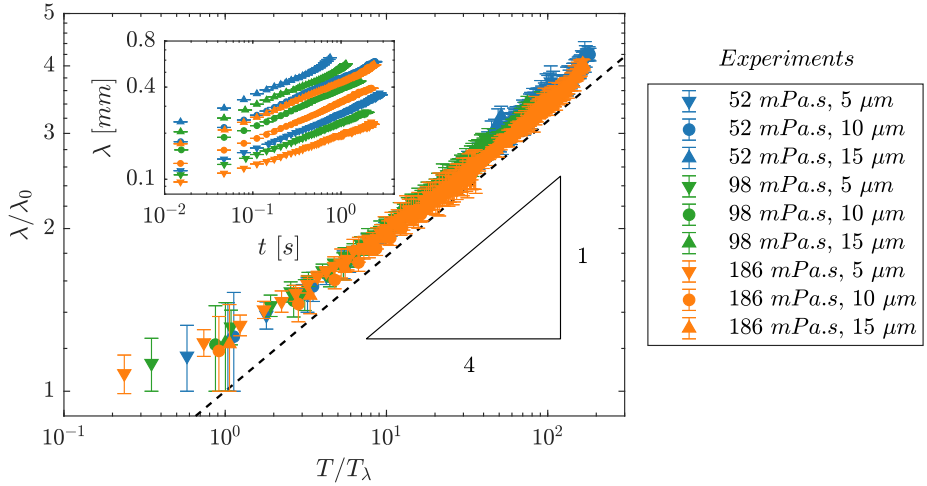


Figure 12: Double logarithmic plot of  $\lambda/\lambda_0$  vs  $T/T_\lambda$ . The mean and errorbar values of  $\lambda/\lambda_0$  are obtained by binning every 25 datapoints. The black dashed line represents  $\lambda/\lambda_0 = (T/T_\lambda)^{1/4}$ .

#### 4.4. Width broadening and amplitude decay

Finally, we will compare theoretical asymptotic scaling laws for the width broadening and amplitude decay with a large number of experiments, all attained for a drop impact velocity of  $v_w \approx 0.16 \text{ m/s}$ . We predict the scaling law for the width  $\lambda$  quantitatively, based on the approach to the attractor function  $\phi_1$ . We formally define the half-width of the similarity function as  $U_1^* = \arg \max |\phi_1(U)| \approx 1.924$ , which is half the absolute distance between global maxima and global minima (cf. Figure 11). From (4.5), we then find

$$\frac{\lambda}{2h_f} \simeq U_1^* T^{1/4}, \quad (4.8)$$

expressing the dimensionless (half) width of the decaying profiles. A practical problem arises when comparing to experiment: at  $t = 0$ , the width takes on a finite value  $\lambda_0$ , so that it is initially incompatible with the from (4.8). To resolve this, we follow Benzaquen *et al.* (2015) and define for each experiment a convergence time  $T_\lambda$  through  $\lambda_0/2h_f = U_1^* T_\lambda^{1/4}$ . The physical meaning of  $T_\lambda$  is that it provides a time at which the experiment should approach the asymptotics power law (4.8). Using this definition of  $T_\lambda$ , the scaling (4.8) then gives

$$\lambda/\lambda_0 \simeq (T/T_\lambda)^{1/4}, \quad (4.9)$$

which can be compared to experiments without adjustable parameters.

In figure 12, we show the temporal dependence  $\lambda/\lambda_0$  vs  $T/T_\lambda$  for different initial film thicknesses and viscosities. The black dashed line in the figure represents Eqn (4.9). Clearly, all experimental data points seem to collapse onto a single master curve which is independent of the film properties used. Moreover, the master curve has a very good agreement with Eqn (4.9). We remark that such a scaling  $\lambda \sim t^{1/4}$  is also seen in previous studies with viscous thin film configurations (Salez *et al.* 2012; McGraw *et al.* 2012; Benzaquen *et al.* 2015; Hack *et al.* 2018).

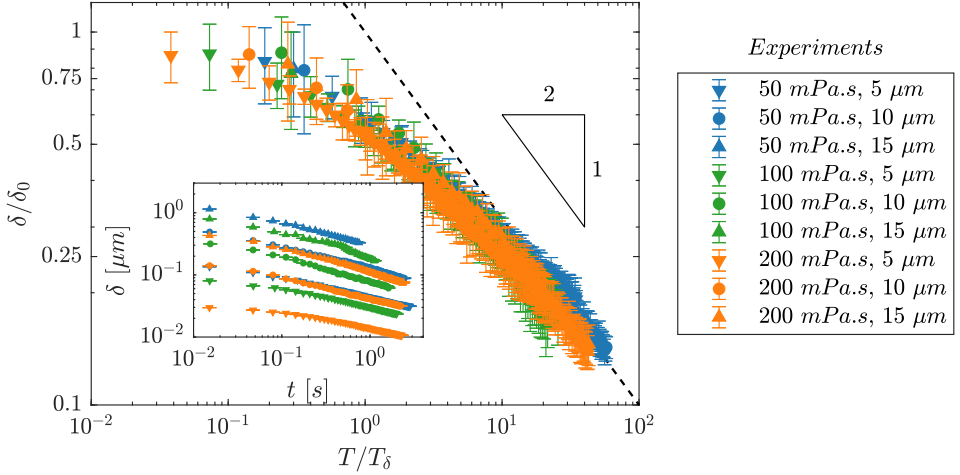


Figure 13: Double logarithmic plot of  $\delta/\delta_0$  vs  $T/T_\delta$ . The mean and errorbar values of  $\delta/\delta_0$  are obtained by binning every 25 datapoints. The black dashed line represents  $\delta/\delta_0 = (T/T_\delta)^{-1/2}$ .

A similar analysis is performed for the amplitude decay. We will once again make use of the self-similar attractor  $\phi_1(U)$  for the relaxation process. Similar to the procedure outlined for the study of the width broadening, we employ Eqn (4.5) which implies,

$$\frac{\delta}{2h_f} \simeq \mathcal{M}_1 \frac{|\phi_1(U^*)|}{T^{1/2}}, \quad (4.10)$$

where  $|\phi_1(U^*)| \approx 0.1164$  is the maximum of the similarity function. To avoid the experimental issue that  $\delta_0$ , the amplitude at  $t = 0$ , is finite, we once again determine for each experiment a convergence time  $T_\delta$ , using  $\delta_0/(2h_f) = \mathcal{M}_1 |\phi_1(U_1^*)|/T_\delta^{1/2}$ . Note that both  $\delta_0$  and  $\mathcal{M}_1$  will be different for each specific experiment, but both parameters can be determined independently. This finally gives that (4.10) can be written as

$$\delta/\delta_0 \simeq (T/T_\delta)^{-1/2}. \quad (4.11)$$

The result for  $\delta/\delta_0$  vs  $T/T_\delta$  for different film thicknesses and different viscosities are shown in Figure 13. The black dashed line in the figure represents Eqn (4.11). While from the individual measurements it is difficult to infer the  $1/2$  scaling law, it is clear that the dashed line captures the correct asymptotics.

## 5. Conclusions and Outlook

In this work, we have performed experiments of a water drop impacting a viscous thin oil film in an ambient air environment. The considered drop impact velocities are restricted to moderately low values  $We \sim 1$  at which drops bounce on thin films caused by an air cushioning effect. The Digital Holographic Microscopy technique has been employed to measure the deformations of the free oil film surface that arise due to the bouncing of drops.

We have first investigated the deformations of the thin film immediately after rebound ( $t = 0$ ) while varying the oil film thickness  $h_f$ , oil viscosity  $\eta_f$ , and the impact velocity

$v_w$  of the drop. We have found that the deformation amplitude after the bounce  $\delta_0$  varies quadratically with oil film thickness  $\delta_0 \sim h_f^2$  and inversely with the oil viscosity  $\delta_0 \sim \eta_f^{-1}$ . Increasing the impact speed from  $v_w \approx 0.16 \text{ m/s}$  to  $v_w \approx 0.37 \text{ m/s}$ , the deformations in the thin film change qualitatively: While at lower speeds, a single annular wavy deformation is found, at higher speeds the radial profiles exhibit two of such depressions and peaks at different radii.

In the second part of the manuscript, we have detailed the relaxation process of the viscous thin films when the drop is far away from the free oil surface after the bounce. Numerical calculations based on lubrication theory using the experimental deformations at  $t = 0$  as initial condition show an excellent match with the experimentally measured evolution of the deformation profiles. Furthermore, we have successfully employed a theoretical analysis developed by [Benzaquen et al. \(2013, 2014, 2015\)](#) to obtain analytical results describing the relaxation process: Taking advantage of the fact that the deformations approach a universal self-similar attractor, the decay of amplitude and growth of width of the deformations can be described without free parameters at late times of the relaxation process. This allows us to collapse the corresponding experimental curves for all different thin film properties investigated.

Measuring the deformations of the falling drop and the viscous thin film simultaneously has proven challenging in the previous literature (cf. [Tang et al. \(2019\)](#)) and in the present experiments. However it is worthwhile to investigate the dynamics of the coupled system as it would allow valuable insight in the formation mechanism of the deformations. To resolve both the drop-air and the oil-air interface, we therefore plan to combine the color interferometry technique by [van der Veen et al. \(2012\)](#), which can be used to extract the narrow air profiles, with the DHM technique described in the present manuscript. In order to understand the formation of the deformations theoretically and quantify possible influences on the macroscopic drop dynamics, the macroscopic impact dynamics have to be coupled to a two layer lubrication model for the air layer and the lubrication layer. Very recently, such an approach has been pursued by [Duchemin & Josserand \(2020\)](#) for drop coalescence with an underlying thin film.

## Acknowledgements

This project has received funding from the European Union’s Horizon 2020 research and innovation programme under the Marie Skłodowska-Curie grant agreement No 722497. The authors thank Kirsten Harth for interesting discussions. Furthermore, the authors thank Michiel Hack for 3D image graphics and Mariia Zhakharova for fabricating PDMS gels.

## Appendix A. Measuring thin film deformations using DHM

Figure 14a shows a schematic diagram where the drop has just moved out of the DHM measuring window after the bounce. The height of the measuring window is roughly  $200 \mu\text{m}$ . Here, we define  $t = 0$  as the first instance when the DHM measuring window is devoid of the water-air interface allowing for a clean measurement of the oil-air deformation. The object beam (consisting of reflection wavefronts from the measuring window) and the reference beam in the DHM interfere to form the holographic pattern recorded by the DHM camera.

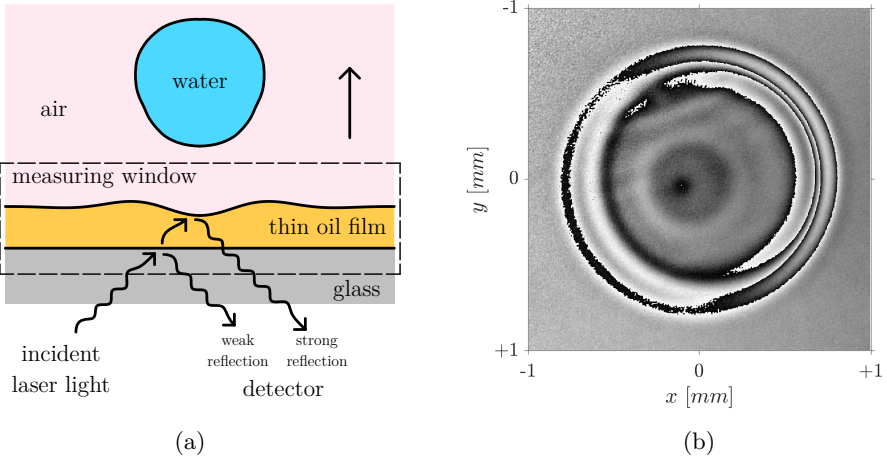


Figure 14: (a) Schematic diagram at  $t = 0$  when the drop has just left the DHM measuring window after the bounce. (b) Phase image of the oil-air deformation at  $t = 0$ . Control parameters used,  $We = 0.38$ ,  $h^* = 0.01$  and  $\eta^* = 98$ .

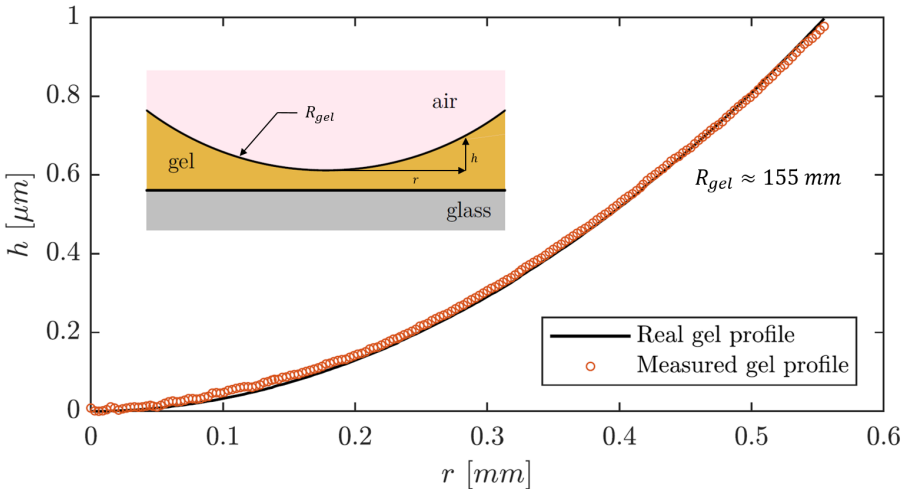


Figure 15: Comparison of thin PDMS gel profiles of a known curvature.

The recorded holograms are converted into their constituent intensity and phase information, wherein the phase information is used to reconstruct the height information. Figure 14b shows an exemplary phase image at time  $t = 0$ . The reconstructed height profile of this phase image is shown in figure 4(a).

To check whether the weak reflection of the glass-oil interface affects the measurements of the oil-air deformation in the bounce experiments, we perform a simple calibration experiment. The calibration experiment is performed to measure the (known) PDMS gel-air profile through glass. Figure 15 shows the comparison of the real and the measured PDMS gel-air deformation. We confirm that the flat glass-PDMS gel interface (and

similarly the flat glass-oil film interface) does not affect the measurements of the thin film deformations. A vertical resolution of around 20 nm is obtained from the calibration plot. It is important to note that the vertical resolution can be well below 20 nm. This is only a conservative estimate since the real PDMS gel profile can suffer from small tilt issues and from surface roughness during its fabrication which are not accounted for here.

## REFERENCES

- BASTIAN, P., BLATT, M., DEDNER, A., ENGWER, C., KLÖFKORN, R., KORNHUBER, R., OHLBERGER, M. & SANDER, O. 2008a A generic grid interface for parallel and adaptive scientific computing. Part II: Implementation and tests in DUNE. *Computing* **82** (2-3), 121–138.
- BASTIAN, P., BLATT, M., DEDNER, A., ENGWER, C., KLÖFKORN, R., OHLBERGER, M. & SANDER, O. 2008b A generic grid interface for parallel and adaptive scientific computing. Part I: abstract framework. *Computing* **82** (2-3), 103–119.
- BASTIAN, P., HEIMANN, F. & MARNACH, S. 2010 Generic implementation of finite element methods in the distributed and unified numerics environment (DUNE). *Kybernetika* **46** (2), 294–315.
- BAUMLI, PHILIPP, TEISALA, HANNU, BAUER, HOIMAR, GARCIA-GONZALEZ, DIANA, DAMLE, VIRAJ, GEYER, FLORIAN, D'ACUNZI, MARIA, KALTBEITZEL, ANKE, BUTT, HANS-JÜRGEN & VOLLMER, DORIS 2019 Flow-induced long-term stable slippery surfaces. *Advanced science* **6** (11), 1900019.
- BENZAQUEN, MICHAEL, FOWLER, PAUL, JUBIN, LAETITIA, SALEZ, THOMAS, DALNOKI-VERESS, KARI & RAPHAL, ELIE 2014 Approach to universal self-similar attractor for the levelling of thin liquid films. *Soft matter* **10** (43), 8608–8614.
- BENZAQUEN, MICHAEL, ILTON, MARK, MASSA, MICHAEL V, SALEZ, THOMAS, FOWLER, PAUL, RAPHAEL, ELIE & DALNOKI-VERESS, KARI 2015 Symmetry plays a key role in the erasing of patterned surface features. *Applied Physics Letters* **107** (5), 053103.
- BENZAQUEN, MICHAEL, SALEZ, THOMAS & RAPHAËL, ELIE 2013 Intermediate asymptotics of the capillary-driven thin-film equation. *The European Physical Journal E* **36** (8), 82.
- BERTIN, VINCENT, NIVEN, JOHN, STONE, HOWARD A, SALEZ, THOMAS, RAPHAEL, ELIE & DALNOKI-VERESS, KARI 2020 Symmetrization of thin freestanding liquid films via a capillary-driven flow. *Physical Review Letters* **124** (18), 184502.
- BOUWHUIS, WILCO, VAN DER VEEN, ROELAND CA, TRAN, TUAN, KEIJ, DIEDERIK L, WINKELS, KOEN G, PETERS, IVO R, VAN DER MEER, DEVARAJ, SUN, CHAO, SNOEIJER, JACCO H & LOHSE, DETLEF 2012 Maximal air bubble entrainment at liquid-drop impact. *Physical review letters* **109** (26), 264501.
- CHANDRA, S & AVEDISIAN, CT 1991 On the collision of a droplet with a solid surface. *Proceedings of the Royal Society of London. Series A: Mathematical and Physical Sciences* **432** (1884), 13–41.
- CHARLES, GO EO & MASON, SO GO 1960 The coalescence of liquid drops with flat liquid/liquid interfaces. *Journal of Colloid Science* **15** (3), 236–267.
- COUDER, YVES, FORT, E, GAUTIER, C-H & BOUDAOU, A 2005a From bouncing to floating: Noncoalescence of drops on a fluid bath. *Physical review letters* **94** (17), 177801.
- COUDER, YVES, PROTIERE, SUZIE, FORT, EMMANUEL & BOUDAOU, AREZKI 2005b Walking and orbiting droplets. *Nature* **437** (7056), 208–208.
- DE RUITER, JOLET, OH, JUNG MIN, VAN DEN ENDE, DIRK & MUGELE, FRIEDER 2012 Dynamics of collapse of air films in drop impact. *Physical review letters* **108** (7), 074505.
- DUCHEMIN, LAURENT & JOSSERAND, CHRISTOPHE 2012 Rarefied gas correction for the bubble entrapment singularity in drop impacts. *Comptes Rendus Mécanique* **340** (11-12), 797–803.
- DUCHEMIN, LAURENT & JOSSERAND, CHRISTOPHE 2020 Dimple drainage before the coalescence of a droplet with a smooth substrate. *arXiv preprint arXiv:2004.12365*.
- GABOR, D. 1949 Microscopy by reconstructed wave-fronts. *Proc. R. Soc. A* **197** (1051), 454–487.
- GAUTHIER, ANAÏS, DIDDENS, CHRISTIAN, PROVILLE, RÉMI, LOHSE, DETLEF & VAN DER

- MEER, DEVARAJ 2019a Self-propulsion of inverse leidenfrost drops on a cryogenic bath. *Proceedings of the National Academy of Sciences* **116** (4), 1174–1179.
- GAUTHIER, ANAËS, VAN DER MEER, DEVARAJ, SNOEIJER, JACCO H & LAJOINIE, GUILLAUME 2019b Capillary orbits. *Nature communications* **10** (1), 1–5.
- GILET, TRISTAN & BUSH, JOHN WM 2012 Droplets bouncing on a wet, inclined surface. *Physics of Fluids* **24** (12), 122103.
- HACK, MA, COSTALONGA, MAXIME, SEGERS, TIM, KARPITSCHKA, STEFAN, WIJSHOFF, HERMAN & SNOEIJER, JH 2018 Printing wet-on-wet: Attraction and repulsion of drops on a viscous film. *Applied physics letters* **113** (18), 183701.
- HAO, CHONGLEI, LI, JING, LIU, YUAN, ZHOU, XIAOFENG, LIU, YAHUA, LIU, RONG, CHE, LUFENG, ZHOU, WENZHONG, SUN, DONG, LI, LAWRENCE & OTHERS 2015 Superhydrophobic-like tunable droplet bouncing on slippery liquid interfaces. *Nature communications* **6** (1), 1–7.
- HENDRIX, MAURICE HW, BOUWHUIS, WILCO, VAN DER MEER, DEVARAJ, LOHSE, DETLEF & SNOEIJER, JACCO H 2016 Universal mechanism for air entrainment during liquid impact. *Journal of fluid mechanics* **789**, 708–725.
- HICKS, PETER D & PURVIS, RICHARD 2010 Air cushioning and bubble entrapment in three-dimensional droplet impacts. *Journal of Fluid Mechanics* **649**, 135–163.
- HICKS, PETER D & PURVIS, RICHARD 2011 Air cushioning in droplet impacts with liquid layers and other droplets. *Physics of fluids* **23** (6), 062104.
- JOSSERAND, CHRISTOPHE & ZALESKI, STAPHANE 2003 Droplet splashing on a thin liquid film. *Physics of Fluids* **15** (6), 1650–1657.
- KLYUZHIN, IVAN S, IENNA, FEDERICO, ROEDER, BRANDON, WEXLER, ADAM & POLLACK, GERALD H 2010 Persisting water droplets on water surfaces. *The Journal of Physical Chemistry B* **114** (44), 14020–14027.
- KOLINSKI, JOHN MARTIN, MAHADEVAN, L & RUBINSTEIN, SM 2014 Drops can bounce from perfectly hydrophilic surfaces. *EPL (Europhysics Letters)* **108** (2), 24001.
- KOLINSKI, JOHN M, RUBINSTEIN, SHMUEL M, MANDRE, SHREYAS, BRENNER, MICHAEL P, WEITZ, DAVID A & MAHADEVAN, L 2012 Skating on a film of air: drops impacting on a surface. *Physical review letters* **108** (7), 074503.
- LANGLEY, KR & THORODDSEN, SIGURDUR T 2019 Gliding on a layer of air: impact of a large-viscosity drop on a liquid film. *Journal of Fluid Mechanics* **878**.
- LI, EQ & THORODDSEN, SIGURDUR T 2015 Time-resolved imaging of a compressible air disc under a drop impacting on a solid surface. *Journal of Fluid Mechanics* **780**, 636–648.
- LO, HAU YUNG, LIU, YUAN & XU, LEI 2017 Mechanism of contact between a droplet and an atomically smooth substrate. *Physical Review X* **7** (2), 021036.
- MANDRE, SHREYAS, MANI, MADHAV & BRENNER, MICHAEL P 2009 Precursors to splashing of liquid droplets on a solid surface. *Physical review letters* **102** (13), 134502.
- MCGRAW, JOSHUA D, SALEZ, THOMAS, BÄUMCHEN, OLIVER, RAPHAËL, ELIE & DALNOKI-VERESS, KARI 2012 Self-similarity and energy dissipation in stepped polymer films. *Physical Review Letters* **109** (12), 128303.
- MOLÁČEK, JAN & BUSH, JOHN WM 2012 A quasi-static model of drop impact. *Physics of Fluids* **24** (12), 127103.
- ORON, ALEXANDER, DAVIS, STEPHEN H & BANKOFF, S GEORGE 1997 Long-scale evolution of thin liquid films. *Reviews of modern physics* **69** (3), 931.
- PACK, MIN, HU, HAN, KIM, D, ZHENG, ZHONG, STONE, HA & SUN, YING 2017 Failure mechanisms of air entrainment in drop impact on lubricated surfaces. *Soft matter* **13** (12), 2402–2409.
- PAN, KUO-LONG & LAW, CHUNG KING 2007 Dynamics of droplet–film collision. *Journal of fluid mechanics* **587**, 1–22.
- QUÉRÉ, DAVID 2013 Leidenfrost dynamics. *Annual Review of Fluid Mechanics* **45**, 197–215.
- RAYLEIGH, LORD 1882 Further observations upon liquid jets, in continuation of those recorded in the royal society's 'proceedings' for march and may, 1879. *Proc. R. Soc. Lond.* **34**, 130–145.
- REIN, MARTIN 1993 Phenomena of liquid drop impact on solid and liquid surfaces. *Fluid Dynamics Research* **12** (2), 61.

- REYNOLDS, O. 1881 On the floating of drops on the surface of water depending only on the purity of the surface. *Proc. Lit. Phil. Soc.* **21** (1), 413–414.
- REYNOLDS, O. 1886 On the theory of lubrication and its application to mr. beauchamp tower's experiments, including an experimental determination of the viscosity of olive oil. *Philos. Trans. Royal Soc.* (177), 157–234.
- RICHARD, DENIS, CLANET, CHRISTOPHE & QUÉRÉ, DAVID 2002 Contact time of a bouncing drop. *Nature* **417** (6891), 811–811.
- RODRIGUEZ, FRANCISCO & MESLER, RUSSELL 1985 Some drops don't splash. *Journal of colloid and interface science* **106** (2), 347–352.
- DE RUITER, JOLET, MUGELE, FRIEDER & VAN DEN ENDE, DIRK 2015 Air cushioning in droplet impact. i. dynamics of thin films studied by dual wavelength reflection interference microscopy. *Physics of fluids* **27** (1), 012104.
- SALEZ, THOMAS, MCGRAW, JOSHUA D, BÄUMCHEN, OLIVER, DALNOKI-VERESS, KARI & RAPHAËL, ELIE 2012 Capillary-driven flow induced by a stepped perturbation atop a viscous film. *Physics of Fluids* **24** (10), 102111.
- SCHELLENBERGER, FRANK, XIE, JING, ENCINAS, NOEMÍ, HARDY, ALEXANDRE, KLAPPER, MARKUS, PAPADOPOULOS, PERIKLIS, BUTT, HANS-JÜRGEN & VOLLMER, DORIS 2015 Direct observation of drops on slippery lubricant-infused surfaces. *Soft Matter* **11** (38), 7617–7626.
- SCHNARS, ULF, FALLDORF, CLAAS, WATSON, JOHN & JÜPTNER, WERNER 2016 *Digital holography and wavefront sensing*. Springer.
- SMITH, FT, LI, L & WU, GX 2003 Air cushioning with a lubrication/inviscid balance. *Journal of Fluid Mechanics* **482**, 291–318.
- TANG, XIAOYU, SAHA, ABHISHEK, LAW, CHUNG K & SUN, CHAO 2018 Bouncing-to-merging transition in drop impact on liquid film: Role of liquid viscosity. *Langmuir* **34** (8), 2654–2662.
- TANG, XIAOYU, SAHA, ABHISHEK, LAW, CHUNG K & SUN, CHAO 2019 Bouncing drop on liquid film: Dynamics of interfacial gas layer. *Physics of Fluids* **31** (1), 013304.
- TEISALA, HANNU, SCHÖNECKER, CLARISSA, KALTBEITZEL, ANKE, STEFFEN, WERNER, BUTT, HANS-JÜRGEN & VOLLMER, DORIS 2018 Wetting over pre-existing liquid films. *Physical Review Fluids* **3** (8), 084002.
- THORODDSEN, ST, ETOH, TG & TAKEHARA, K 2003 Air entrapment under an impacting drop. *Journal of Fluid Mechanics* **478**, 125–134.
- THORODDSEN, ST, ETOH, TG & TAKEHARA, K 2008 High-speed imaging of drops and bubbles. *Annu. Rev. Fluid Mech.* **40**, 257–285.
- THORODDSEN, ST, ETOH, TG, TAKEHARA, K, OOTSUKA, N & HATSUKI, Y 2005 The air bubble entrapped under a drop impacting on a solid surface. *Journal of Fluid Mechanics* **545**, 203–212.
- TRAN, TUAN, DE MALEPRADE, HÉLÈNE, SUN, CHAO & LOHSE, DETLEF 2013 Air entrainment during impact of droplets on liquid surfaces. *Journal of Fluid Mechanics* **726**.
- VAN DER VEEN, ROELAND CA, TRAN, TUAN, LOHSE, DETLEF & SUN, CHAO 2012 Direct measurements of air layer profiles under impacting droplets using high-speed color interferometry. *Physical Review E* **85** (2), 026315.
- WEISS, DANIEL A & YARIN, ALEXANDER L 1999 Single drop impact onto liquid films: neck distortion, jetting, tiny bubble entrainment, and crown formation. *Journal of Fluid Mechanics* **385**, 229–254.
- WORTHINGTON, A. M. 1908 *A study of splashes*. London: Longman, Green and Co.
- XU, LEI, ZHANG, WENDY W & NAGEL, SIDNEY R 2005 Drop splashing on a dry smooth surface. *Physical review letters* **94** (18), 184505.